Lawrence Berkeley National Laboratory

Title

Estimating Permafrost Distribution Using Co-Located Temperature and Electrical Resistivity Measurements

Permalink

https://escholarship.org/uc/item/9v34322z

Journal

Geophysical Research Letters, 50(17)

ISSN

0094-8276

Authors

Uhlemann, S
Shirley, I
Wielandt, S
et al.

Publication Date

2023-09-16

DOI

10.1029/2023gl103987

Copyright Information

Peer reviewed

Estimating Permafrost Distribution Using Co-Located Temperature and Electrical Resistivity Measurements

S. Uhlemann[1] , I. Shirley[1] , S. Wielandt[1], C. Ulrich[1], C. Wang[1], S. Fiolleau[1] , J. Peterson[1], J. Lamb[1,2], E. Thaler[3], J. Rowland[3] , S. S. Hubbard[1,4] , and B. Dafflon[1]

[1]Earth and Environmental Sciences Area, Lawrence Berkeley National Laboratory, Berkeley, CA, USA, [2]Stanford University, Palo Alto, CA, USA, [3]Division of Earth and Environmental Sciences, Los Alamos National Laboratory, Los Alamos, NM, USA, [4]Oak Ridge National Laboratory, Oak Ridge, TN, USA

Abstract Assessing the lateral and vertical extent of permafrost is critical to understanding the fate of Arctic ecosystems under climate change. Yet, direct measurements of permafrost distribution and temperature are often limited to a small number of borehole locations. Here, we assess the use of co-located shallow temperature and electrical resistivity tomography (ERT) measurements to estimate at high-resolution the distribution of permafrost in three watersheds underlain by discontinuous permafrost. Synthetic modeling shows that co-located temperature and ERT measurements allow for supervised classification schemes that provide 60% higher accuracy compared to unsupervised methods. Linking resistivity and size of the identified permafrost bodies to surface observations, we show that tall vegetation (>0.5 m) and gentle slopes (<15°) are related to warmer and smaller permafrost bodies, and a more frequent occurrence of taliks.

Plain Language Summary To better understand how the Arctic may be changing due to climate warming, we need to understand the distribution of permafrost in the subsurface. Although the temperatures of the ground can be measured in boreholes, only a small number of boreholes exist to do these measurements. Here, we use machine learning to link measurements of temperature and of the electrical resistivity of the ground to obtain detailed distributions of permafrost in the subsurface. Connecting the properties of permafrost with observations above ground, we show that south facing slopes, tall vegetation, and gentle slopes relate to warmer and smaller permafrost bodies.

1. Introduction

The Arctic is known to be a critical driver of the global response to climate change (Cohen et al., 2014). Thawing of permafrost causes emission of greenhouse gases, but also changes the Arctic ecosystem, leading to shrub expansion and increasing forest sizes (Danby & Hik, 2007; Myers-Smith et al., 2011). On global scales, permafrost distribution can be approximated using remote sensing and modeling approaches (Gruber, 2012; Li et al., 2022). However locally, permafrost distribution can be highly heterogeneous, driven by variations in vegetation, snow distribution, and soil properties (Jorgenson et al., 2010; Smith et al., 2022). Such variability, and its impact on hydrology, is a critical driver in Arctic landscape and ecosystem transitions (Grosse et al., 2011; Rowland et al., 2010). Hence, understanding permafrost distribution and evolution is critical to understanding the Arctic's response to increasing mean annual temperatures, and the subsequent effect on the Arctic carbon stocks (Schuur et al., 2015).

Measurements of subsurface temperatures are the most direct way of estimating permafrost distribution and thickness. Borehole temperature measurements in Alaska have shown permafrost thicknesses ranging between as little as 5 m in, for example, coastal areas of the Seward Peninsula to more than 600 m close to Prudhoe Bay (Jorgenson et al., 2008). While borehole temperatures and other geophysical logs can be measured relatively easily, interpreting them can be difficult, and permafrost thickness obtained from borehole measurements are estimated to be accurate within ±10 m (Osterkamp & Payne, 1981). Additionally, drilling the boreholes to make these measurements is difficult due to remote locations and challenging subsurface materials; hence only a limited number of direct observations of permafrost thickness exist and estimating the spatial distribution of permafrost from these sparse measurements is difficult. In contrast, improved accuracy of low-cost thermal sensors have led to dense spatial measurements of the shallow thermal dynamics of permafrost systems (Dafflon et al., 2022) that enable high-resolution mapping of permafrost distribution and estimation of soil thermal properties (Brunetti

Methodology: S. Uhlemann, I. Shirley, S. Wielandt, C. Ulrich, C. Wang, S. Fiolleau, J. Peterson, J. Lamb, J. Rowland, B. Dafflon
Project Administration: J. Rowland, S. S. Hubbard, B. Dafflon
Supervision: J. Rowland, S. S. Hubbard, B. Dafflon
Validation: S. Uhlemann
Visualization: S. Uhlemann
Writing – original draft: S. Uhlemann
Writing – review & editing: I. Shirley, S. Wielandt, C. Ulrich, C. Wang, S. Fiolleau, J. Peterson, J. Lamb, E. Thaler, J. Rowland, S. S. Hubbard, B. Dafflon

et al., 2022). While these shallow measurements are easy to obtain, they may fail in accurately mapping permafrost with a thick active layer and do not provide information on the permafrost thickness.

Geophysical imaging techniques have been shown to overcome these limitations by providing spatially resolved subsurface property distributions that are proxies to the thermal state of permafrost. Electrical properties are often used to map permafrost landscapes, because the electrical resistivity of the subsurface below the freezing point is impacted by the remaining amount of unfrozen water, and thus a proxy to subsurface temperature (Hauck, 2002; Uhlemann et al., 2021; Wu et al., 2017). Electrical resistivity tomography (ERT) has been used to map permafrost spatial distribution and depth (Arboleda-Zapata et al., 2022; Minsley et al., 2012; Tran et al., 2018; You et al., 2013), as well as ice-content if petrophysical relationships and site conditions allow for it (Dafflon et al., 2017). Geophysical imaging has also been used to investigate permafrost dynamics, and has shown that lateral flow may have a significant contribution to the formation of taliks (Uhlemann et al., 2021) and that disturbances, such as wildfires, have a spatially variable and long-term impact on permafrost systems (Minsley et al., 2022).

While geophysical techniques have been used successfully to map the spatial distribution of permafrost bodies and even their temporal dynamics, mapping of the extent of permafrost remains challenging. There are three main obstacles to assessing permafrost extent: (a) geophysical imaging relies on inversion techniques to recover the subsurface property distribution, which are non-unique processes that require smoothing and usually have decreasing resolution with increasing depth, (b) geophysical properties are often proxies to the thermal state of the subsurface and are also influenced by other parameters (such as lithology), and (c) deep boreholes that can be used to relate geophysical parameters to the base of permafrost are rare. Hence, there is a need for co-located measurements of temperature and electrical resistivity to reduce the ambiguity of both methods. Here, we present an approach that makes use of such co-located measurements to obtain both the spatial distribution and thickness of permafrost bodies in a highly heterogeneous discontinuous permafrost environment. Using unsupervised learning, we estimate the spatial distribution of permafrost, and use this distribution as input for supervised learning to estimate the permafrost thickness.

2. Materials and Methods

2.1. The Seward Peninsula—A Discontinuous Permafrost Environment

We focus on three watersheds on the southern Seward Peninsula, Alaska, USA, a region that is characterized by discontinuous permafrost and presents a rapidly changing landscape and ecosystem (Debolskiy et al., 2020; Sulman et al., 2021). While currently about 70% of the southern Seward peninsula is underlain by permafrost, by the end of the century it is projected that the extent will reduce to less than 10% (Debolskiy et al., 2020), likely causing major hydrologic and ecologic changes. Two of the watersheds are located along the Nome-Teller Highway (along mile markers 27 and 47, referred to as T27 and T47, respectively), and one is located north–east of the Kigluaik mountains, at Kougarok road (mile marker 64, referred to as KG, Figure 1a). Temperature measurements obtained at 0.8 m depth across each watershed indicate late summer mean temperatures of 3.1, 2.3, and 0.7°C for T27, T47, and KG, respectively, which relate to a decreasing trend in mean annual air temperature with increasing latitude and distance to the ocean. Thaw layer thickness varies considerably in this environment, ranging from 0.5 to more than 2 m depth (i.e., deeper than common tile probe). T27 consists mostly of a south–east facing slope, covered by graminoid and dwarf/tall shrubs in the lower (south) and mid elevation, and a wetland complex with significant micro-topography in the upper elevation (north). T47 consists of south, east, and north–east facing slopes, separated by two streams that merge toward the bottom of the watershed (Figure 1b). The site is mostly covered by tussock tundra, dwarf shrubs and grasses with patches of tall shrubs, particularly near the streams (Del Vecchio et al., 2022), and outcropping bedrock at the highest elevations. KG is the site that is farthest inland. The slopes are covered with tussock tundra in the lower elevation, tall shrubs at mid-elevation and bare-ground where a granitic intrusion is outcropping at the highest elevations (Salmon et al., 2019). Geologically, the sites are comparable with a thin layer of organic material (0.3–0.5 m thick) overlying silty material of varying thickness laying above schist (T27 and T47) or granitic (KG) bedrock. At each site, we acquired co-located ERT and distributed temperature measurements in late summers of 2018 (T27), 2019 (KG), 2021 (T47), and 2022 (T27).

2.2. Distributed Temperature Measurements

Depth-resolved soil temperature data were acquired using a custom-made distributed temperature probe (DTP), which is described in detail in Dafflon et al. (2022). The DTP consists of an array of high-resolution digital temperature sensors at 0.05 m spacing inside an epoxy filled 0.8 m long, 10 mm outer diameter stainless steel tube (Dafflon
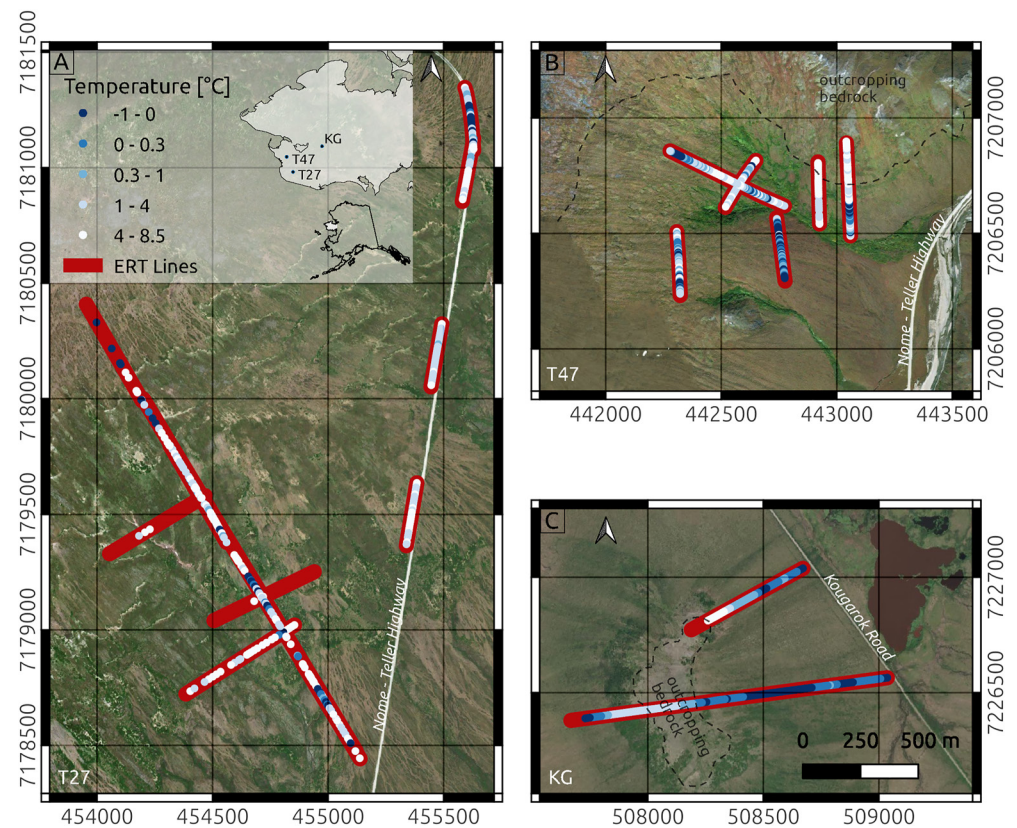
Figure 1. Overview map showing the distribution of late summer temperature measurements at 0.8 m depth (blue to white dots), and the location of electrical resistivity tomography profiles (red lines) on top of aerial photographs (coordinate system UTM Zone 3N) for the watersheds T27 (a), T47 (b), and KG (c). The inset in (a) shows the location of the sites in Alaska and on the Seward Peninsula. Aerial photographs from BING (T27 and T47), and ESRI Imagery (KG).

et al., 2022). In-house evaluation of the temperature sensors showed that recorded temperature values are accurate within ±0.07°C. The DTPs were pushed into the ground where possible, or inserted into a pre-drilled hole of equal diameter to the probes OD. Before taking the reading, probes were allowed to equilibrate for at least 30 min. Each measurement location was surveyed using GNSS RTK positioning. Spacing between measurement locations was either 5 or 10 m. At T27, in addition to measurements taken at the same time as the ERT data acquisition, we made use of a network of soil temperature monitoring locations. The sample locations are shown in Figure 1. At all locations, we extracted the temperature at 0.8 m depth, and calculated the temperature gradient between 0.6 and 0.8 m depth.

2.3. Electrical Resistivity Tomography

The electrical resistance of the ground is measured using two pairs of electrodes, where one pair is used to inject a current into the ground and a second pair is used to measure a voltage (Binley & Kemna, 2005). By varying the locations of the electrode pairs, the subsurface is sampled at various locations and depths. Here, we used either 96 or 112 electrodes spaced at 2 m, and acquired dipole-dipole data with dipole lengths a of 2, 4, 6, 8, 10, and 12 m, and dipole spacing n of 1–6 a. To obtain the resistivity distribution of the subsurface, the resistance measurements need to be inverted. We used ResIPy (Blanchy et al., 2020) to pre-process and invert the data. Pre-processing included data filtering based on the reciprocal errors, and deriving of a data error model (Tso et al., 2017). Data were inverted using an L2 norm in both the data and model space. Inversions converged to a χ^2 misfit of 1, meaning that the model fits the data within their errors. The survey locations are indicated in Figure 1.

2.4. Unsupervised and Supervised Clustering

We used an unsupervised classification method to determine the location of near-surface permafrost. Input data for the classification are the standardized temperature at 0.8 m depth and the standardized mean of the $\log_{10}$
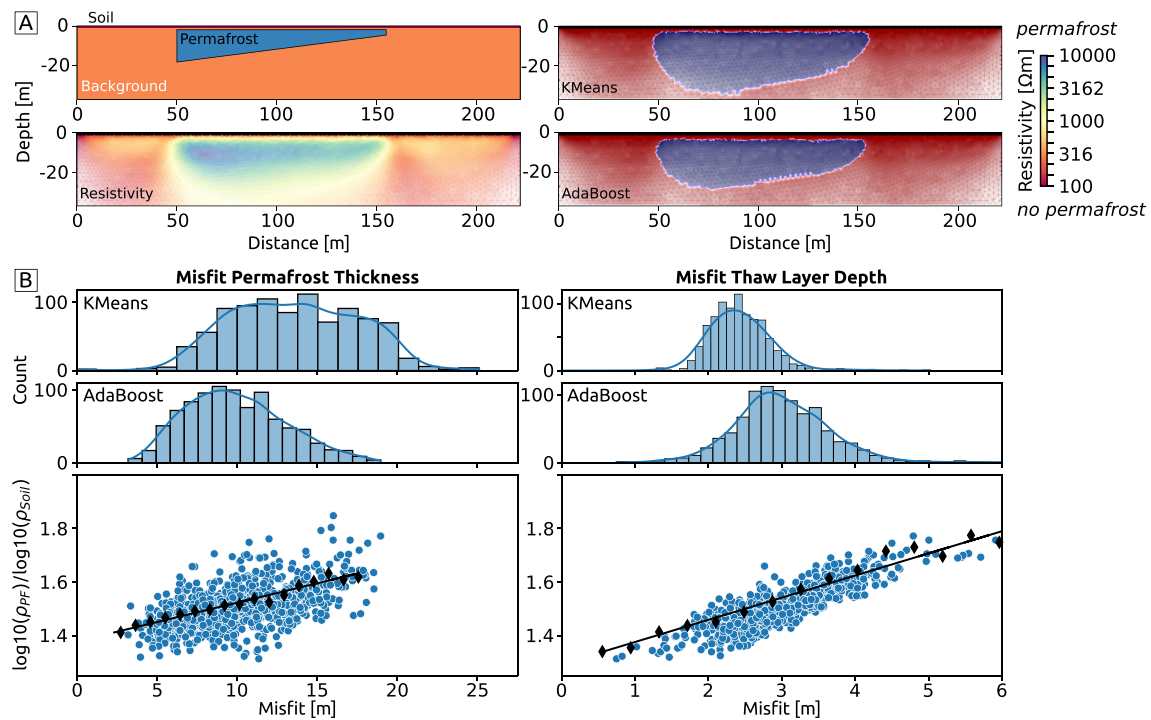
Figure 2. Accuracy of predicting the size of permafrost bodies from electrical resistivity tomography (ERT) data. (a) Resistivity model and inversion result (left), and classified images for unsupervised kMeans and supervised AdaBoost classifiers (right). Note that the sensitivity of the ERT inversion is used to blend out unreliable data. (b) Analysis of 1,000 model realization with varying soil, background, and permafrost resistivities with regards to permafrost thickness (left) and depth to the permafrost table (right). Misfit distributions are shown for kMeans and AdaBoost; bottom row shows a scatter plot of misfit and $\log_{10}$ resistivity ratio between the permafrost body and the soil layer. Black diamonds show binned mean values, used for estimating the linear relationship.

resistivity between 1 and 3 m depth. Although data are spatially co-located, the deeper resistivities were chosen to avoid potential near surface effects, and shallow temperatures are assumed to be indicative of conditions at 1–3 m depth. Data were classified using a weighted kMeans approach implemented in scikit-learn (Pedregosa et al., 2011), where $|T_s - 1|$ was used as weights, with T_s being the min-max scaled temperature measurements, resulting in higher weights on the colder temperatures.

To estimate the size of the permafrost bodies, we used the near-surface permafrost locations classified from the co-located temperature and resistivity measurements, and extracted the mean of the $\log_{10}$ resistivity at 5–10 m depth at these locations, to classify the presence or absence of permafrost throughout the ERT imaging plane. These deeper training resistivities were chosen because they reflect the conditions of the permafrost bodies better than the shallower values, and hence provided improved performance. These data sets were standardized and used as training data. Both unsupervised (training on the resistivity distribution only) and supervised classification (training on resistivity and near surface permafrost location) were tested. For the unsupervised classification kMeans was used, and for the supervised classification the AdaBoost-SAMME algorithm (Hastie et al., 2009; Pedregosa et al., 2011).

Although ERT has been used to map the extent of permafrost bodies (Buddo et al., 2022; McClymont et al., 2013), it is also known that these estimates have a high uncertainty (Arboleda-Zapata et al., 2022). We assess the uncertainty of the unsupervised and supervised classification methods through forward modeling of a range of model scenarios. We created a representative model, with a permafrost wedge having an active layer thickness of 1.5 m, and a thickness varying from 5 to 15 m (see Figure 2). The modeled permafrost body sits within a background material that is overlain by 0.5 m of low resistivity organic or soil material, which reflects our field conditions where saturated, low resistivity organic material and soil overlie more resistive silt and bedrock. We calculated the response of 1,000 different models, for which we randomly drew resistivity values for each model domain. Each domain followed a normal distribution with a mean of 50 Ωm and standard deviation of 15 Ωm for the soil layer, a mean of 500 Ωm and standard deviation of 100 Ωm for the background, and a mean of 10,000 Ωm and standard deviation of 5,000 Ωm for the permafrost layer. Forward modeling was performed on a very finely

discretized mesh using ResIPy. The modeled data were inverted using the same parameters as used for the field data.

2.5. Linking Subsurface and Surface Features

We extracted the permafrost bodies from the classified ERT models, corrected their size using the results of the synthetic study, and calculated their center and length-to-thickness ratio, their mean thaw layer depth and permafrost resistivity, and extracted the mean slope aspect and gradient, and the mean vegetation height for each permafrost body from LiDAR data that were acquired by the National Center for Airborne Laser Mapping in August 2021 (Singhania, 2021). The LiDAR point clouds were processed to generate a digital elevation model, with the vegetation removed using the lidR package (Roussel et al., 2020). DEMs were produced at 3 m spatial resolution. We classified the aspect to be north, east, south, and west facing. Only two permafrost bodies were on west facing slopes and zero on north facing slopes, and hence, we removed them from the following analysis. The slope gradient was simplified to reflect whether a slope was steep (>15°) or not. Similarly, vegetation was classified as being tall if their height was >0.5 m.

3. Results and Discussion

3.1. Assessing the Prediction Accuracy

The results of the synthetic study show that both kMeans and AdaBoost overestimate the depth to the thaw layer and the depth to the base of the permafrost (Figure 2b). For the thaw layer depth, kMeans has a smaller mean misfit than AdaBoost (2.2 and 3.0 m, respectively), but for the permafrost thickness, the kMeans misfit is 4.8 m larger than for AdaBoost (means of 13.9 and 9.1 m, respectively), and the misfit distribution of kMeans is also considerably wider (standard deviation of 7.2 and 3.9 m, respectively). An ≈60% greater accuracy of the supervised classification method indicates the substantial improvement in mapping permafrost bodies by utilizing co-located temperature and resistivity data.

The overestimation depends on the resistivity contrast between the permafrost layer, and the soil and background resistivities, and is most pronounced for the contrast between permafrost and soil layers (Figure 2b). The larger the contrast, the higher the misfit, which we associate to a loss in sensitivity and an overfitting of the inversion process. Our analysis also showed that the resistivity contrast has a stronger impact on the misfit than the actual thickness of the permafrost layer, that is, the misfit was almost constant along the permafrost wedge for each resistivity contrast. The estimate of the thaw layer depth and permafrost thickness can be corrected by fitting a linear relationship to the misfit values and the resistivity contrast. This correction has been applied to the field data.

We also analyzed the impact of blocky inversion constraints (L1 model norm, Figure S1 in Supporting Information S1), and tested the known-interface method (Chambers et al., 2013), which uses a resistivity threshold based on prior information for extracting the base of the permafrost (Figure S2 in Supporting Information S1). However, the blocky inversion did not provide better performance for estimating permafrost thickness, and the resistivity threshold considerably underestimated the size of the permafrost body (more detail in Supporting Information S1).

3.2. Estimating Lateral Extent of Permafrost

Soil temperatures usually show a bimodal distribution, where T47 has a more pronounced low temperature peak (0.2°C) compared to T27, for which the higher temperature peak (4.7°C) is more prominent (Figure 3a). KG, although showing a second high temperature peak, is characterized mostly by low temperatures centered around 0.05°C. Since the resistivity is related to the temperature, KG and T47 are also characterized by higher intermediate depth resistivities (1–3 m) than T27 (1,375, 671, and 608 Ωm, respectively). Shallower resistivities (0–1 m) showed a similar trend, while the deeper resistivities (5–10 m) show distributions that are more closely aligned (2,512, 2,004, and 1,202 Ωm for KG, T47, and T27, respectively).

Using the co-located resistivity and temperature values (Uhlemann et al., 2023), a weighted kMeans classifier was trained with a silhouette score of 0.53 (Figure 3b). We assume that the temperature at 0.8 m depth is related to
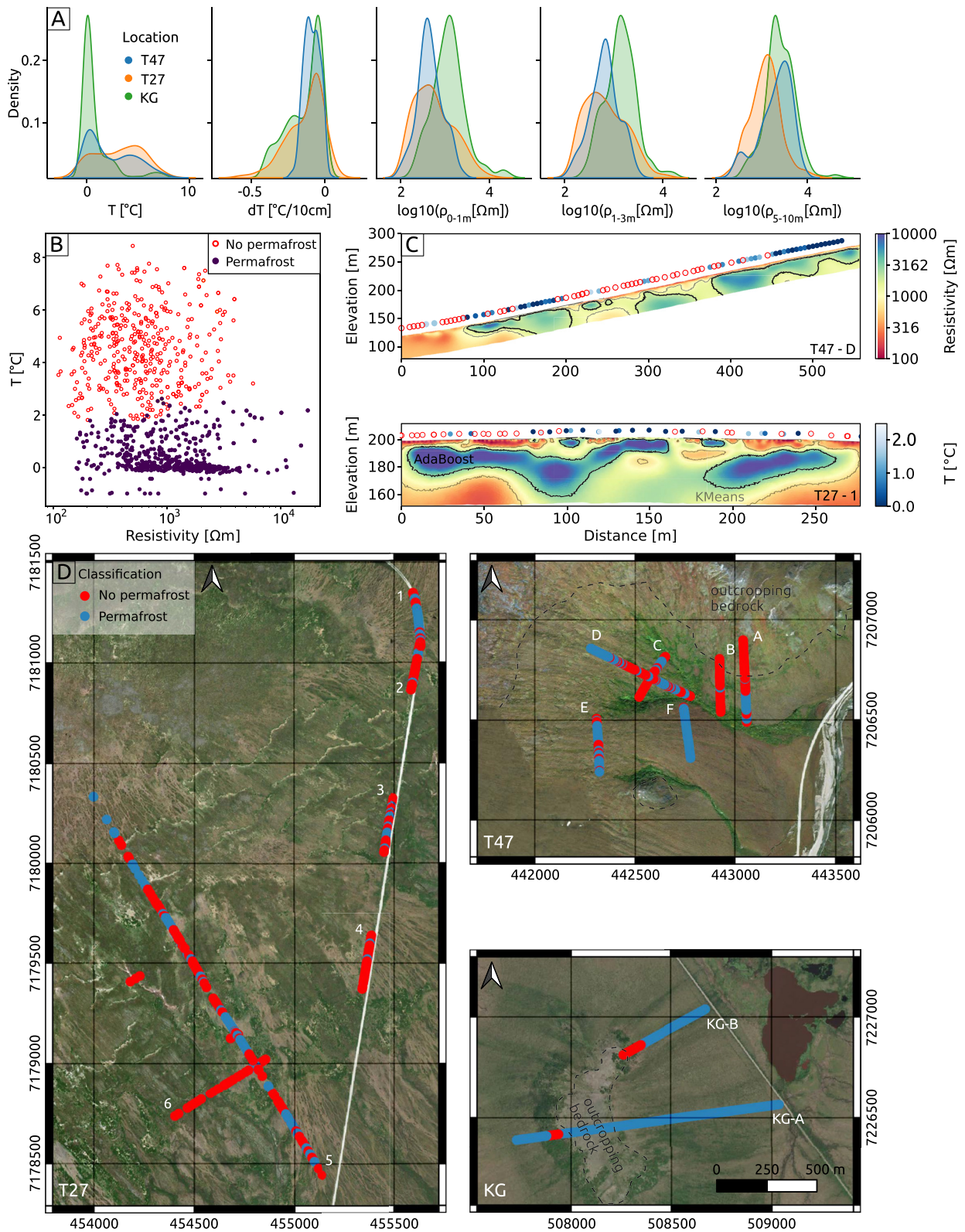
Figure 3.

deeper soil temperatures, and acknowledge that the temperature at this depth is not only controlled by the thermal conditions, but also hydrological processes. Hence, also temperatures above 0°C may be representative for deeper permafrost conditions, which is shown by the results of the classification. Samples are classified as permafrost if their temperature is less than 1.8°C, but this temperature threshold can be as high as 2.4°C if resistivities are >3,000 Ωm. We also tested including the temperature gradient into the classification, but no improved classification score was achieved. Plotting the clustering results along the transects of ERT and temperature data, we find that identified permafrost locations correlate well with locations of shallow high resistivity anomalies and low soil temperatures (Figure 3c). However, this method is not able to identify the presence of deeper resistive bodies that we assume to be permafrost (e.g., ≈300 m at T47-D).

The spatial distribution shows that T27 is characterized by isolated permafrost occurrences, which mostly relate to areas dominated by graminoid, and a wetland complex in the upper elevations. For T47, permafrost mostly occurs at the western part of the site, on south–east and north–east facing slopes (transects C—F), while south-facing slopes show only isolated near-surface permafrost (transects A and B). Note that the north-eastern part of the site is characterized by outcropping bedrock, which may have a deep active layer or no permafrost. KG shows the largest fraction of mapped permafrost, which covers almost the entire site, except for some small areas that are linked to outcropping bedrock and a south–west facing slope. Although soil temperatures were comparably high in the western part of transect KG-A, it was predominantly classified as permafrost, mostly due to the very high resistivities recorded at that site. Hence, this area is either misclassified, or the site is characterized by a thick active layer on top of frozen bedrock.

### 3.3. Mapping Permafrost Thickness

The synthetic example has shown that a higher accuracy can be achieved when using supervised rather than unsupervised classification. An AdaBoost model was trained to classify permafrost occurrences on the ERT data, using the resistivity at 5–10 m depth and the estimated permafrost occurrence as input data. We trained a model for each site to account for variations in the geological settings. Validating against test data (input data were randomly split into a training (70%) and test data (30%)), the AdaBoost model has an accuracy of 69.7%, compared to 62.4% for a standard kMeans model. The AdaBoost classification outlines high resistivity bodies (Figure 3), which relate well with mapped locations of low soil temperatures when close to the surface. The kMeans classification predicts permafrost to occupy larger areas, and often identifies near-surface permafrost in areas where no low soil temperatures were measured. This shows that co-located temperature and resistivity measurements can be used to obtain reliable estimates of subsurface permafrost distribution.

South-facing slopes generally have a larger thaw layer than east-facing slopes (mean of 1.2 and 0.3 m, respectively, Figure 4a), and a smaller mean resistivity (2,100 and 2,900 Ωm, respectively), indicating warmer permafrost temperatures. Both observations are expected for the northern hemisphere, where south-facing slopes receive larger solar radiation than east-facing slopes. We analyzed the $\log_{10}$ of the length-to-thickness ratio, which indicates horizontally elongated bodies if >0 and vertically elongated bodies if <0. Predominantly vertically elongated bodies can be associated with more frequent through taliks and discontinuous permafrost features, while horizontally elongated bodies show more spatial continuity. More horizontally elongated permafrost bodies can be found for east-facing slopes, while south-facing slopes show a considerably larger fraction of vertically elongated features. Permafrost was absent at 57.8% on south-facing slopes, while for east-facing slopes only 39.5% had no permafrost. Assuming that the absence of permafrost can be related to the occurrence of through taliks, this shows a significantly larger presence of through taliks on south-facing than on east-facing slopes.

Parameter distributions vary across the three sites, but the variations in aspect outweigh inter-site variability. Decreasing late summer soil temperatures (T27 warmest and KG coldest site) lead to more horizontally elongated and hence more spatially continuous permafrost bodies. This is also obvious from the permafrost fraction of each site, where permafrost accounts for 37.8%, 40.1%, and 70.3% at T27, T47, and KG, respectively. T27, generally, shows the largest variability, highlighting the heterogeneous conditions at this site. Results suggest a spatially

Figure 3. Estimating permafrost distribution. (a) Distribution of characteristic variables for each watershed, including the soil temperature at 0.8 m depth, the temperature gradient between 0.6 and 0.8 m depth, and the mean resistivity between 0 and 1 m, 1 and 3 m, and 5 and 10 m depth. (b) Cross-plot of resistivity at 1–3 m depth, and soil temperature, showing the clustering results. (c) Electrical resistivity tomography models for T47-D and T27-1, showing the temperature sampling locations, including the measured temperature (blue to white colored fill of dots) and their permafrost classification (red outline meaning no permafrost). Shown are also the estimated permafrost bodies, where solid black line outlines the AdaBoost classification, and the gray outline the KMeans classification. (d) Spatial distribution of permafrost classification for the three studied watersheds. Aerial photographs from BING (T27 and T47), and ESRI Imagery (KG).
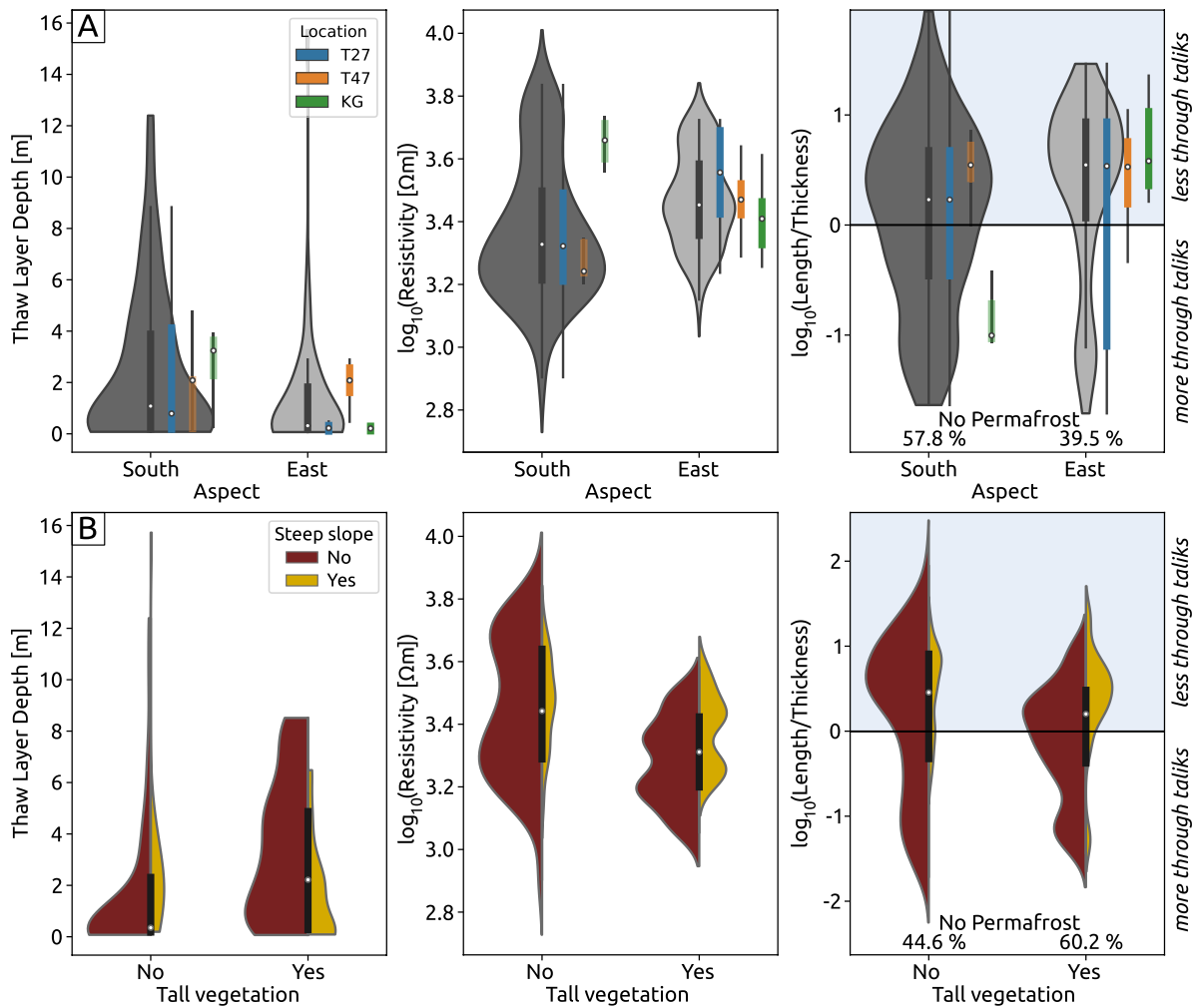
Figure 4. Characteristics of identified permafrost bodies. (a) Thaw layer depth, permafrost mean resistivity, and $\log_{10}$ of the length-to-thickness ratio of the permafrost bodies. Colored boxplots indicate the mean and standard deviation for each studied watershed. Note that for T47 and KG, the sample size for south facing permafrost bodies is small (5 and 4, respectively). (b) Distributions of thaw layer depth, mean resistivity and length-to-thickness ratio divided by whether tall vegetation (>0.5 m) occurs above the body, and whether it is located on a steep slope (>15°). The fraction of no permafrost occurrence for south and east facing slopes, and below low and tall vegetation is also given.

varying connection between shallow and deep subsurface temperatures across and within the studied watersheds, which likely results from the complex coupling of atmospheric, surface, and subsurface processes to the deep subsurface temperatures (Jorgenson et al., 2010; Vasiliev et al., 2020). Overall, the higher mean annual temperature of T27 results in a more discontinuous permafrost environment, as highlighted by the broad distribution of length-to-thickness ratio of the identified permafrost bodies.

Vegetation is a major control on snow distribution in Arctic environments, where tall vegetation usually relates to thick snowpack (Bennett et al., 2022; Sturm et al., 2001). The insulating snowpack is known to be a driver for talik formation and increasing permafrost thaw rate (Farquharson et al., 2022; Jafarov et al., 2018; Shirley et al., 2022). At our sites, permafrost bodies below tall vegetation (>0.5 m) had a deeper thaw layer, were of lower resistivity (i.e., warmer), and generally less spatially continuous (smaller length-to-thickness ratio) compared to permafrost bodies covered by low vegetation, highlighting that the snow insulation effect is leading to smaller and warmer permafrost. The link between tall shrub and warm soil conditions is also clear when calculating the fraction of the surveyed area with no permafrost, where absence of permafrost below tall vegetation accounted for 60.2%, and below low vegetation for 44.6%.

Analyzing the characteristics of permafrost bodies with regards to the slope gradient shows that steep slopes tend to be underlain by more resistive, that is, colder, and larger, spatially continuous permafrost. The warmer

and spatially more heterogeneous conditions below gentle slopes could be caused by increased surface water accumulation on gentle or flat slopes that is leading to an increased energy input and hence increased thaw rate (McKenzie & Voss, 2013; Rowland et al., 2011). The potential effect of accumulating water is also expressed by a decreasing resistivity of the permafrost bodies with decreasing distance to the closest water body for each watershed (see Figure S3 in Supporting Information S1). Finally, we note here that spatial variability in geology remains a source of uncertainty in delineating permafrost. For example, shallow bedrock implying large thermal conductivity that may lead to a deep thaw layer, could be misinterpreted as permafrost bodies due to its high resistivity, or deeper frozen bedrock could be interpreted as unfrozen, even when incorporating co-located measurements.

4. Summary

Knowing the distribution, extent, and state of permafrost bodies is crucial for predicting the evolution of Arctic ecosystems and associated environmental changes (Kreplin et al., 2021; Loranty et al., 2018). Here, we developed a novel method that couples temperature and ERT data to estimate permafrost thickness and spatial distribution. We show that co-located temperature and resistivity measurements and their combined data analysis reduce the ambiguity of interpreting each method independently, particularly in cases of deep thaw layer depths or outcropping bedrock. Analyzing the identified permafrost bodies with regards to surface features, we show that permafrost below south-facing slopes tends to be warmer (i.e., less resistive) and smaller than below east-facing slopes, and that there is a larger fraction of through taliks on south-facing slopes. Permafrost bodies are also warmer and smaller below tall vegetation, and on gentle or flat slopes ($<15°$), highlighting the impact of snow accumulation at tall vegetation, and increased surface water—groundwater interaction that is expected on the more gentle slopes.

Data Availability Statement

The temperature and electrical resistivity data analyzed in this study are published on the NGEE Arctic Data Collection (Uhlemann et al., 2023). Topographic indices were calculated from LiDAR data published as Singhania (2021). Forward and inverse modeling of the electrical resistivity tomography data were performed using ResIPy (Blanchy et al., 2020). Figures were prepared using Matplotlib version 3.6.2 (Caswell et al., 2022).

References

Arboleda-Zapata, M., Angelopoulos, M., Overduin, P. P., Grosse, G., Jones, B. M., & Tronicke, J. (2022). Exploring the capabilities of electrical resistivity tomography to study subsea permafrost. *The Cryosphere*, 16(10), 4423–4445. https://doi.org/10.5194/tc-16-4423-2022

Bennett, K. E., Miller, G., Busey, R., Chen, M., Lathrop, E. R., Dann, J. B., et al. (2022). Spatial patterns of snow distribution in the sub-Arctic. *The Cryosphere*, 16(8), 3269–3293. https://doi.org/10.5194/tc-16-3269-2022

Binley, A., & Kemna, A. (2005). DC resistivity and induced polarization methods. In *Hydrogeophysics* (pp. 129–156).

Blanchy, G., Saneiyan, S., Boyd, J., McLachlan, P., & Binley, A. (2020). ResIPy, an intuitive open source software for complex geoelectrical inversion/modeling. *Computers & Geosciences*, 137, 104423. https://doi.org/10.1016/j.cageo.2020.104423

Brunetti, C., Lamb, J., Wielandt, S., Uhlemann, S., Shirley, I., McClure, P., & Dafflon, B. (2022). Probabilistic estimation of depth-resolved profiles of soil thermal diffusivity from temperature time series. *Earth Surface Dynamics*, 10(4), 687–704. https://doi.org/10.5194/esurf-10-687-2022

Buddo, I., Misyurkeeva, N., Shelokhov, I., Chuvilin, E., Chernikh, A., & Smirnov, A. (2022). Imaging arctic permafrost: Modeling for choice of geophysical methods. *Geosciences*, 12(10), 389. https://doi.org/10.3390/geosciences12100389

Caswell, T. A., Lee, A., Droettboom, M., de Andrade, E. S., Hoffmann, T., Klymak, J., et al. (2022). matplotlib/matplotlib: Rel: v3.6.2 [Software]. Zenodo. https://doi.org/10.5281/zenodo.7275322

Chambers, J., Wilkinson, P., Penn, S., Meldrum, P., Kuras, O., Loke, M., & Gunn, D. (2013). River terrace sand and gravel deposit reserve estimation using three-dimensional electrical resistivity tomography for bedrock surface detection. *Journal of Applied Geophysics*, 93, 25–32. https://doi.org/10.1016/j.jappgeo.2013.03.002

Cohen, J., Screen, J. A., Furtado, J. C., Barlow, M., Whittleston, D., Coumou, D., et al. (2014). Recent arctic amplification and extreme mid-latitude weather. *Nature Geoscience*, 7(9), 627–637. https://doi.org/10.1038/ngeo2234

Dafflon, B., Oktem, R., Peterson, J., Ulrich, C., Tran, A. P., Romanovsky, V., & Hubbard, S. S. (2017). Coincident aboveground and below-ground autonomous monitoring to quantify covariability in permafrost, soil, and vegetation properties in arctic tundra. *Journal of Geophysical Research: Biogeosciences*, 122(6), 1321–1342. https://doi.org/10.1002/2016JG003724

Dafflon, B., Wielandt, S., Lamb, J., McClure, P., Shirley, I., Uhlemann, S., et al. (2022). A distributed temperature profiling system for vertically and laterally dense acquisition of soil and snow temperature. *The Cryosphere*, 16(2), 719–736. https://doi.org/10.5194/tc-16-719-2022

Danby, R. K., & Hik, D. S. (2007). Variability, contingency and rapid change in recent subarctic alpine tree line dynamics. *Journal of Ecology*, 95(2), 352–363. https://doi.org/10.1111/j.1365-2745.2006.01200.x

Debolskiy, M. V., Nicolsky, D. J., Hock, R., & Romanovsky, V. E. (2020). Modeling present and future permafrost distribution at the Seward Peninsula, Alaska. *Journal of Geophysical Research: Earth Surface*, 125(8), e2019JF005355. https://doi.org/10.1029/2019JF005355

Del Vecchio, J., Lathrop, E., Dann, J. B., Andresen, C. G., Collins, A. D., Fratkin, M. M., et al. (2022). Patterns and rates of soil movement and shallow failures across several small watersheds on the Seward Peninsula, Alaska. *Earth Surface Dynamics Discussions*, 1–28. https://doi.org/10.5194/esurf-2022-43

Farquharson, L. M., Romanovsky, V. E., Kholodov, A., & Nicolsky, D. (2022). Sub-aerial talik formation observed across the discontinuous permafrost zone of Alaska. *Nature Geoscience*, *15*(6), 475–481. https://doi.org/10.1038/s41561-022-00952-z

Grosse, G., Romanovsky, V., Jorgenson, T., Anthony, K. W., Brown, J., & Overduin, P. P. (2011). Vulnerability and feedbacks of permafrost to climate change. *Eos, Transactions American Geophysical Union*, *92*(9), 73–74. https://doi.org/10.1029/2011EO090001

Gruber, S. (2012). Derivation and analysis of a high-resolution estimate of global permafrost zonation. *The Cryosphere*, *6*(1), 221–233. https://doi.org/10.5194/tc-6-221-2012

Hastie, T., Rosset, S., Zhu, J., & Zou, H. (2009). Multi-class adaboost. *Statistics and Its Interface*, *2*(3), 349–360. https://doi.org/10.4310/sii.2009.v2.n3.a8

Hauck, C. (2002). Frozen ground monitoring using dc resistivity tomography. *Geophysical Research Letters*, *29*(21), 2016. https://doi.org/10.1029/2002GL014995

Jafarov, E. E., Coon, E. T., Harp, D. R., Wilson, C. J., Painter, S. L., Atchley, A. L., & Romanovsky, V. E. (2018). Modeling the role of preferential snow accumulation in through talik development and hillslope groundwater flow in a transitional permafrost landscape. *Environmental Research Letters*, *13*(10), 105006. https://doi.org/10.1088/1748-9326/aadd30

Jorgenson, M. T., Romanovsky, V., Harden, J., Shur, Y., O'Donnell, J., Schuur, E. A. G., et al. (2010). Resilience and vulnerability of permafrost to climate change. *Canadian Journal of Forest Research*, *40*(7), 1219–1236. https://doi.org/10.1139/X10-060

Jorgenson, M. T., Yoshikawa, K., Kanevskiy, M., Shur, Y., Romanovsky, V., Marchenko, S., et al. (2008). Permafrost characteristics of Alaska. *Proceedings of the ninth international conference on permafrost* (Vol. 3, pp. 121–122).

Kreplin, H. N., Ferreira, C. S. S., Destouni, G., Keesstra, S. D., Salvati, L., & Kalantari, Z. (2021). Arctic wetland system dynamics under climate warming. *WIREs Water*, *8*(4). https://doi.org/10.1002/wat2.1526

Li, G., Zhang, M., Pei, W., Melnikov, A., Khristoforov, I., Li, R., & Yu, F. (2022). Permafrost extent and active layer thickness variation in the Northern Hemisphere from 1969 to 2018. *Science of the Total Environment*, *804*, 804. https://doi.org/10.1016/j.scitotenv.2021.150182

Loranty, M. M., Abbott, B. W., Blok, D., Douglas, T. A., Epstein, H. E., Forbes, B. C., et al. (2018). Reviews and syntheses: Changing ecosystem influences on soil thermal regimes in northern high-latitude permafrost regions. *Biogeosciences*, *15*(17), 5287–5313. https://doi.org/10.5194/bg-15-5287-2018

McClymont, A. F., Hayashi, M., Bentley, L. R., & Christensen, B. S. (2013). Geophysical imaging and thermal modeling of subsurface morphology and thaw evolution of discontinuous permafrost. *Journal of Geophysical Research: Earth Surface*, *118*(3), 1826–1837. https://doi.org/10.1002/jgrf.20114

McKenzie, J. M., & Voss, C. I. (2013). Permafrost thaw in a nested groundwater-flow system. *Hydrogeology Journal*, *21*(1), 299–316. https://doi.org/10.1007/s10040-012-0942-3

Minsley, B. J., Abraham, J. D., Smith, B. D., Cannia, J. C., Voss, C. I., Jorgenson, M. T., et al. (2012). Airborne electromagnetic imaging of discontinuous permafrost. *Geophysical Research Letters*, *39*(2), 1–8. https://doi.org/10.1029/2011GL050079

Minsley, B. J., Pastick, N. J., James, S. R., Brown, D. R. N., Wylie, B. K., Kass, M. A., & Romanovsky, V. E. (2022). Rapid and gradual permafrost thaw: A tale of two sites. *Geophysical Research Letters*, *49*(21), e2022GL100285. https://doi.org/10.1029/2022GL100285

Myers-Smith, I. H., Forbes, B. C., Wilmking, M., Hallinger, M., Lantz, T., Blok, D., et al. (2011). Shrub expansion in tundra ecosystems: Dynamics, impacts and research priorities. *Environmental Research Letters*, *6*(4), 045509. https://doi.org/10.1088/1748-9326/6/4/045509

Osterkamp, T. E., & Payne, M. W. (1981). Estimates of permafrost thickness from well logs in northern Alaska (Vol. *5*).

Pedregosa, F., Varoquaux, G., Gramfort, A., Michel, V., Thirion, B., Grisel, O., et al. (2011). Scikit-learn: Machine learning in Python. *Journal of Machine Learning Research*, *12*, 2825–2830.

Roussel, J.-R., Auty, D., Coops, N. C., Tompalski, P., Goodbody, T. R., Meador, A. S., et al. (2020). lidR: An R package for analysis of airborne laser scanning (ALS) data. *Remote Sensing of Environment*, *251*, 112061. https://doi.org/10.1016/j.rse.2020.112061

Rowland, J. C., Jones, C. E., Altmann, G., Bryan, R., Crosby, B. T., Hinzman, L. D., et al. (2010). Arctic landscapes in transition: Responses to thawing permafrost. *Eos, Transactions American Geophysical Union*, *91*(26), 229–230. https://doi.org/10.1029/2010EO260001

Rowland, J. C., Travis, B. J., & Wilson, C. J. (2011). The role of advective heat transport in talik development beneath lakes and ponds in discontinuous permafrost. *Geophysical Research Letters*, *38*(17), L17504. https://doi.org/10.1029/2011GL048497

Salmon, V. G., Breen, A. L., Kumar, J., Lara, M. J., Thornton, P. E., Wullschleger, S. D., & Iversen, C. M. (2019). Alder distribution and expansion across a tundra hillslope: Implications for local N cycling. *Frontiers in Plant Science*, *10*. https://doi.org/10.3389/fpls.2019.01099

Schuur, E. A. G., McGuire, A. D., Schädel, C., Grosse, G., Harden, J. W., Hayes, D. J., et al. (2015). Climate change and the permafrost carbon feedback. *Nature*, *520*(7546), 171–179. https://doi.org/10.1038/nature14338

Shirley, I. A., Mekonnen, Z. A., Wainwright, H., Romanovsky, V. E., Grant, R. F., Hubbard, S. S., et al. (2022). Near-surface hydrology and soil properties drive heterogeneity in permafrost distribution, vegetation dynamics, and carbon cycling in a Sub-Arctic watershed. *Journal of Geophysical Research: Biogeosciences*, *127*(9), e2022JG006864. https://doi.org/10.1029/2022JG006864

Singhania, A. (2021). National center for airborne laser mapping (NCALM) lidar DEM data from five NGEE Arctic sites, Seward Peninsula, Alaska, august 2021 [Dataset]. Next Generation Ecosystem Experiments Arctic Data Collection, Oak Ridge National Laboratory, U.S. Department of Energy. https://doi.org/10.5440/1832016

Smith, S. L., O'Neill, H. B., Isaksen, K., Noetzli, J., & Romanovsky, V. E. (2022). The changing thermal state of permafrost. *Nature Reviews Earth & Environment*, *3*(1), 10–23. https://doi.org/10.1038/s43017-021-00240-1

Sturm, M., Holmgren, J., McFadden, J. P., Liston, G. E., Chapin, F. S., & Racine, C. H. (2001). Snow–shrub interactions in arctic tundra: A hypothesis with climatic implications. *Journal of Climate*, *14*(3), 336–344. https://doi.org/10.1175/1520-0442(2001)014<0336:SSIIAT>2.0.CO;2

Sulman, B. N., Salmon, V. G., Iversen, C. M., Breen, A. L., Yuan, F., & Thornton, P. E. (2021). Integrating arctic plant functional types in a land surface model using above- and belowground field observations. *Journal of Advances in Modeling Earth Systems*, *13*(4), e2020MS002396. https://doi.org/10.1029/2020MS002396

Tran, A. P., Dafflon, B., Bisht, G., & Hubbard, S. S. (2018). Spatial and temporal variations of thaw layer thickness and its controlling factors identified using time-lapse electrical resistivity tomography and hydro-thermal modeling. *Journal of Hydrology*, *561*, 751–763. https://doi.org/10.1016/j.jhydrol.2018.04.028

Tso, C.-H. M., Kuras, O., Wilkinson, P. B., Uhlemann, S., Chambers, J. E., Meldrum, P. I., et al. (2017). Improved characterization and modelling of measurement errors in electrical resistivity tomography (ERT) surveys. *Journal of Applied Geophysics*, *146*, 103–119. https://doi.org/10.1016/j.jappgeo.2017.09.009

Uhlemann, S., Dafflon, B., Peterson, J., Ulrich, C., Shirley, I., Michail, S., & Hubbard, S. S. (2021). Geophysical monitoring shows that spatial heterogeneity in thermohydrological dynamics reshapes a transitional permafrost system. *Geophysical Research Letters*, *48*(6), e2020GL091149. https://doi.org/10.1029/2020GL091149

Uhlemann, S., Dafflon, B., Ulrich, C., Peterson, J., Shirley, I., Wielandt, S., et al. (2023). Co-located temperature and electrical resistivity measurements for permafrost mapping, teller 27, teller 47 and Kougarok 64, Seward Peninsula, Alaska, late summers of 2018, 2019, 2021, and 2022 [Dataset]. Next Generation Ecosystem Experiments Arctic Data Collection, Oak Ridge National Laboratory, U.S. Department of Energy. https://doi.org/10.5440/1987841

Vasiliev, A. A., Drozdov, D. S., Gravis, A. G., Malkova, G. V., Nyland, K. E., & Streletskiy, D. A. (2020). Permafrost degradation in the western Russian arctic. *Environmental Research Letters*, *15*(4), 045001. https://doi.org/10.1088/1748-9326/ab6f12

Wu, Y., Nakagawa, S., Kneafsey, T. J., Dafflon, B., & Hubbard, S. (2017). Electrical and seismic response of saline permafrost soil during freeze—Thaw transition. *Journal of Applied Geophysics*, *146*, 16–26. https://doi.org/10.1016/j.jappgeo.2017.08.008

You, Y., Yu, Q., Pan, X., Wang, X., & Guo, L. (2013). Application of electrical resistivity tomography in investigating depth of permafrost base and permafrost structure in Tibetan plateau. *Cold Regions Science and Technology*, *87*, 19–26. https://doi.org/10.1016/j.coldregions.2012.11.004